

1 **Advancing Our Understanding of Martian Proton Aurora through a**
2 **Coordinated Multi-Model Comparison Campaign**
3

4 **Andréa C. G. Hughes^{1,2,3}, Michael Chaffin⁴, Edwin Mierkiewicz³, Justin Deighan⁴, Rebecca**
5 **D. Jolitz⁴, Esa Kallio⁵, Guillaume Gronoff^{6,7}, Valery Shematovich⁸, Dmitry Bisikalo^{8,9},**
6 **Jasper Halekas¹⁰, Cyril Simon Wedlund¹¹, Nicholas Schneider⁴, Birgit Ritter^{12,13}, Zachary**
7 **Girazian¹⁰, Sonal Jain⁴, Jean-Claude Gérard¹², and Bradley Hegyi^{6,7}**

8 ¹ NASA Goddard Space Flight Center, Greenbelt, MD, United States.

9 ² Department of Physics & Astronomy, Howard University, Washington, DC, United States.

10 ³ Center for Space and Atmospheric Research (CSAR) and the Department of Physical Sciences,
11 Embry-Riddle Aeronautical University, Daytona Beach, Florida, United States.

12 ⁴ Laboratory for Atmospheric and Space Physics, University of Colorado, Boulder, CO, USA.
13 United States.

14 ⁵ Aalto University, School of Electrical Engineering, Department of Electronics and
15 Nanoengineering, Espoo, Finland.

16 ⁶ NASA Langley Research Center, Hampton, VA, United States.

17 ⁷ Science Systems and Application Inc. Hampton, VA, United States.

18 ⁸ Institute of Astronomy of the Russian Academy of Sciences, Moscow, Russia.

19 ⁹ National Center for Physics and Mathematics, Russian Federation, Moscow, Russia.

20 ¹⁰ Department of Physics and Astronomy, University of Iowa, Iowa City, IA, United States.

21 ¹¹ Space Research Institute, Austrian Academy of Sciences, Graz, Austria.

22 ¹² Royal Observatory of Belgium, Brussels, Belgium.

23 ¹³ Université de Liège, LPAP – STAR Institute, Liege, Belgium.

24
25 Corresponding author (first): Andrea Hughes (Andrea.C.Hughes@NASA.gov)

26 Corresponding author (second): Michael Chaffin (Michael.Chaffin@colorado.edu)
27

28 **Key Points:**

- 29 ● We undertake a multi-model comparison campaign to gain a better understanding of the
30 physics and driving processes of Martian proton aurora
31 ● The incident solar wind particle flux and velocity are found to be the two most influential
32 parameters affecting the proton aurora profile

- 33 • The models effectively reproduce observations, with variations due to different model
34 capabilities/solving techniques and input assumptions

35

36 **Abstract**

37 Proton aurora are the most commonly observed yet least studied type of aurora at Mars. In
38 order to better understand the physics and driving processes of Martian proton aurora, we
39 undertake a multi-model comparison campaign. We compare results from four different
40 proton/hydrogen precipitation models with unique abilities to represent Martian proton aurora:
41 Jolitz model (3-D Monte Carlo), Kallio model (3-D Monte Carlo), Bisikalo/Shematovich *et al.*
42 model (1-D kinetic Monte Carlo), and Gronoff *et al.* model (1-D kinetic). This campaign is
43 divided into two steps: an inter-model comparison and a data-model comparison. The inter-
44 model comparison entails modeling five different representative cases using similar constraints
45 in order to better understand the capabilities and limitations of each of the models. Through this
46 step we find that the two primary variables affecting proton aurora are the incident solar wind
47 particle flux and velocity. In the data-model comparison, we assess the robustness of each model
48 based on its ability to reproduce a MAVEN/IUVS proton aurora observation. All models are able
49 to effectively simulate the data. Variations in modeled intensity and peak altitude can be
50 attributed to differences in model capabilities/solving techniques and input assumptions (*e.g.*,
51 cross sections, 3-D versus 1-D solvers, and implementation of the relevant physics and
52 processes). The good match between the observations and multiple models gives a measure of
53 confidence that the appropriate physical processes and their associated parameters have been
54 correctly identified, and provides insight into the key physics that should be incorporated in
55 future models.

56

57 Plain Language Summary

58 The purpose of the present study is to gain a deeper understanding of the physics and
59 driving processes of Martian proton aurora through a comparative modeling campaign. The
60 models involved in this study have important similarities and differences, such as the
61 dimensionality (*e.g.*, 3-D versus 1-D), inputs, and relevant physics included. We separate the
62 modeling campaign into two steps: a first step comparing the models with each other (*i.e.*,
63 model-model comparison), and a second step comparing the simulated model results with data
64 from a proton aurora observation (*i.e.*, data-model comparison) taken by the Imaging UltraViolet
65 Spectrograph (IUVS) onboard the Mars Atmosphere and Volatile Evolution (MAVEN)
66 spacecraft. We find that all of the models are able to effectively simulate the data in terms of
67 shape and brightness range of the proton aurora observation. The results of this study inform our
68 understanding of the primary influencing factors that cause variability in the Martian proton
69 aurora profile, the effects of dynamically changing solar wind parameters on the coupled Mars-
70 Sun auroral system (*e.g.*, through extreme solar events such as coronal mass ejections and solar
71 wind stream interactions), and the physical processes/constraints that should be considered in
72 future modeling attempts of this unique phenomenon.

73

74 1. Introduction and Background

75 Proton aurora have been recently determined to be the most commonly observed type of
76 aurora at Mars (Hughes *et al.*, 2019). This form of aurora is one of three primary types of
77 Martian aurora, in addition to discrete (Bertaux *et al.*, 2005) and diffuse aurora (Schneider *et al.*,
78 2015). Further, even though this phenomenon was theoretically predicted by Kallio and Barabash
79 (2001), proton aurora is the most recently discovered type of Martian aurora (Deighan *et al.*,
80 2018; Ritter *et al.*, 2018), and is thereby arguably one of the least studied and understood types
81 of Martian aurora. Past efforts to model these phenomena have been unable to fully reproduce
82 the observations (*e.g.*, Deighan *et al.*, 2018, in which the shape of the modeled profile resembled
83 the data, but the modeled peak altitudes were consistently below the data and modeled intensities
84 required adjustment via a scaling factor to match the data), suggesting a gap in our understanding
85 and a need for further exploration of the underlying physics of these events through modeling.

86 Proton aurora can be identified in ultraviolet data as an enhancement in the hydrogen (H)
87 Lyman-alpha ($\text{Ly-}\alpha$) emission (121.6 nm) above the background coronal H brightness between
88 an altitude of ~ 110 -150 km; this enhancement is due to the contribution from the proton aurora-
89 inducing H energetic neutral atoms (ENAs) as they collide with the atmosphere and emit photons
90 (see Figure 1 from Hughes *et al.*, 2019 for more detail and explanation of formation processes).
91 In a previous statistical study, Hughes *et al.* (2019) used multiple Mars years of data from the
92 Imaging UltraViolet Spectrograph (IUVS) (McClintock *et al.*, 2015) onboard the Mars
93 Atmosphere and Volatile Evolution (MAVEN) spacecraft (Jakosky *et al.*, 2015) to assess the
94 phenomenology of Martian proton aurora. Based on this study, they found that most Martian
95 proton aurora events occur on the dayside of the planet (*i.e.*, at low solar zenith angles, SZAs)
96 around the southern summer solstice (*i.e.*, solar longitude, L_s , $\sim 270^\circ$). This seasonal increase in
97 proton aurora activity was found to be correlated with the inflated Martian H corona around
98 southern summer solstice, which corresponds with higher H column densities and H escape rates,
99 caused by upper atmospheric temperatures and dust activity reaching an annual maximum during
100 this time (*e.g.*, Hughes *et al.*, 2019; Chaffin *et al.*, 2021; Chaffin *et al.*, 2014; Clarke *et al.*, 2014;
101 Halekas, 2017). This annual variability is also coupled with slightly higher solar wind proton
102 fluxes as Mars is near perihelion ($L_s = 251^\circ$). The seasonally increased abundance of H beyond
103 the planet's bow shock during this season allows a larger fraction of solar wind protons to be
104 converted into hydrogen ENAs (H-ENAs) (*i.e.*, through charge exchange), which can then
105 bypass the bow shock and magnetic pileup boundary to create more frequent proton aurora
106 events with very large $\text{Ly-}\alpha$ emission enhancements during this time of year.

107 The purpose of the present study is to gain a deeper understanding of the physics and
108 driving processes of Martian proton aurora through a comparative modeling campaign. While
109 previous data-driven statistical studies of these aurora provided an understanding of their
110 phenomenology, frequency, and likely driving processes, much is still lacking in our knowledge.
111 This includes, for example, the specific effects of variability in different input parameters on the
112 shape, brightness, and peak altitude of the proton aurora profile, as well as the influence of
113 model capabilities, solving techniques, and input assumptions on effectively simulating proton
114 aurora observations. Modeling proton aurora activity provides an opportunity to understand these
115 events, as it allows us to constrain different input parameters and predict variations in the results.
116 Moreover, by undertaking a comparative modeling campaign in which the results of multiple
117 models are evaluated (with each model emphasizing specific physical processes and utilizing
118 different numerical solving techniques), we are able to simultaneously explore the range of

119 possible outcomes for individual auroral events. We note that the statistical study by Hughes *et*
120 *al.* (2019) incorporated data from only the first ~two Mars years of MAVEN orbits, taken during
121 the declining and minimum portion of the solar cycle. While the Hughes *et al.* (2019) study
122 encompassed many proton aurora events, in this study we focus our efforts on modeling one
123 specific event from the IUVS dataset that exhibited particularly interesting proton aurora
124 activity.

125 Being able to effectively model Martian proton aurora is necessary for developing our
126 understanding of observations of auroral events in the IUVS dataset, as well as the ability to
127 predict and understand future observations. The purpose of this modeling campaign is not to
128 determine which model is the “best” proton/hydrogen precipitation model in our study, but rather
129 to identify the distinct capabilities each model provides in simulating proton/hydrogen
130 precipitation at Mars. Through undertaking a rigorous assessment of Martian proton aurora using
131 the results of multiple different simulations, we are able to develop an understanding of the gaps
132 in our knowledge and improve our abilities to more effectively model future proton aurora
133 observations.

134 2. Modeling Campaign Description

135 2.1. Campaign Outline/Steps

136 In order to accomplish the goals of this study, this campaign is divided into two primary
137 steps: an inter-model comparison step (Step 1) and a data-model comparison step (Step 2). Each
138 step is subdivided to reflect the “native format” (*i.e.*, original model outputs) and “forward-
139 modeled” (*i.e.*, after running model outputs through radiative transfer model – described in more
140 detail below) results (*i.e.*, Steps 1-A and 1-B, as well as Steps 2-A and 2-B). In the following
141 sections we describe the models and discuss the results of each of these steps. We also consider
142 the assumptions of each model and compare differences in the model capabilities (*e.g.*, the
143 physics represented in each model) that may impact the results.

144 2.2. Models and Modeling Teams Involved in Campaign

145 In this study we utilize four different proton/hydrogen precipitation models and one
146 radiative transfer model. Here we briefly discuss the different models and teams involved.
147 Detailed descriptions of each of the four proton/hydrogen precipitation models used in the study
148 and an overview table comparing their cross section assumptions are provided in supplementary
149 material (Text S1-S4 and Table S1). A radiative transfer (RT) model is then used to “forward-
150 model” the results of each step into observation space (*i.e.*, Steps 1-B and 2-B, respectively); this
151 model is also briefly described below.

152 2.2.1. Proton/Hydrogen Precipitation Models

153 We include four unique proton/hydrogen precipitation models in this study: the Jolitz
154 model (*i.e.*, “ASPEN”), the Kallio model, the Bisikalo/Shematovich *et al.* model, and the
155 Gronoff *et al.* model (*i.e.*, “Aeroplanets”). The former three are Monte Carlo (MC) models (with
156 the Jolitz and Kallio models being 3-dimensional (3-D) and the Bisikalo/Shematovich *et al.*
157 model being 1-D). A MC simulation is a numerical technique that generates a range of possible
158 outcomes and probabilities of occurrence for specific representative inputs. In such a simulation,
159 a mathematical model is first constructed and then iteratively run using different random input

160 variables; the results can be considered in the context of a probability distribution curve and are
161 averaged together to estimate the most likely outcome. In contrast, the Gronoff *et al.* model uses
162 a 1-D Kinetic scheme, based on a semi-analytical treatment of the coupled H⁺/H Boltzmann
163 kinetic transport equation.

164 2.2.1.1. *Jolitz 3-D Monte Carlo model (“ASPEN”)*

165 The Jolitz model, *i.e.*, ASPEN (Atmospheric Scattering of Protons, Electrons, and
166 Neutrals), is a 3-D Monte Carlo test particle simulation. This model was initially developed to
167 predict atmospheric ionization rates at Mars by solar energetic particles, which have higher
168 energies than the ENAs studied in this paper (Jolitz *et al.*, 2017), and has since been used to
169 predict precipitating SEP electron fluxes at Mars (Jolitz *et al.*, 2021). The model solves the
170 Lorentz force equations for energetic particle motion and uses a Monte Carlo approach to predict
171 collisions and resulting energy loss in the atmosphere.

172 Using ASPEN, stochastic collisions are modeled by inverting the relation between
173 intensity, density, and absorption cross section for a particle beam incident on a medium of
174 scatterers (colloquially known as Beer’s law) to dynamically calculate a probability distribution
175 function that is combined with a random number to predict variable distances between collisions.
176 This probability distribution function is calculated for each individual particle and depends on
177 the position, path, and energy through the planetary atmosphere. Similarly, whenever a collision
178 occurs, the type of collision is predicted probabilistically using the relative cross section of each
179 possible collisional process and the particle energy is decremented by the corresponding energy
180 loss. As a particle loses energy, the relative cross sections of each process change.

181 This model (as well as all models in this study) is highly dependent on the choice of cross
182 sections. For the application in this study, the selected cross sections for hydrogen and proton
183 impact on carbon dioxide are described in Jolitz *et al.* (2017), with one exception: the cross
184 sections for proton- and hydrogen-impact excitation was replaced with Ly- α emission cross
185 sections. ASPEN uses a cross section calculated by scaling the corresponding emission cross
186 sections from impact on molecular oxygen.

187 Since ASPEN is a 3-D Monte Carlo simulation, predicting an accurate emission rate
188 requires appropriate choice of initial conditions and a large volume of simulated particles. For
189 Step 1, we simulate 10,000 particles incident on the subsolar point from an altitude of 600 km
190 and calculated the emission rate by binning all Ly- α emitting collisions as a function of altitude
191 and multiplying by the incident flux. For Step 2, we simulate 10,000 particles uniformly
192 distributed in space on a plane perpendicular to the direction of solar wind flow. Each particle
193 represents a fraction of the assumed incident flux. The emission rate was then calculated by
194 weighing the total number of emissions binned by altitude, solar zenith angle, and the fraction of
195 flux associated with each simulated particle.

196 2.2.1.2. *Kallio 3-D Monte Carlo model*

197 The Kallio model is a 3-D Monte Carlo model where the incident particle, either H⁺ or H,
198 collides with neutral particles, after which the velocity of the particle is changed. The model
199 includes 6 elastic and 24 inelastic processes; however, in this study, only the processes
200 mentioned in the main text of this paper were used.

201 The model inputs are neutral atom densities, energy dependent total cross sections, the
202 differential scattering cross sections (DSCS), the number of precipitating particles (5,000
203 particles in the Step 1 runs and 100,000 particles in Step 2 runs), and the initial positions and
204 velocities of the precipitating particles (in the present case hydrogen atoms). The total cross
205 sections are given in Kallio and Barabash (2001, Table 1 and Fig. 3) and the DSCS scattering
206 angle distribution in Kallio and Barabash (2000, Fig. 1, “nominal”) and Kallio and Barabash
207 (2001, Fig. 2). Total cross sections give the probability that a collision occurs. Random numbers
208 are used to model if a collision occurs, and which collision process occurs. If a collision happens,
209 then the DSCS determines the new velocity of the incident particle after collision. The value of
210 the scattering angle is obtained by using a new random variable.

211 The largest uncertainty for the obtained Ly- α volume emission rate is related to the
212 uncertainty of the total cross sections used and the DSCS between H and H⁺ particles and CO₂
213 molecules. In the simulation many of these H/H⁺ collisions with CO₂ are modeled with H/H⁺
214 collisions with O₂ and N₂ which was published in the literature (see Kallio and Barabash, 2001,
215 Table 1, for details).

216 In the simulation, particles are injected into the upper atmosphere at the point $[x, y, z] =$
217 $[260 \text{ km} + R_{\text{Mars}}, 0, 0]$, where the radius of Mars, R_{Mars} , is 3393 km. The model saves the position
218 and the velocity of the particle if it has a Ly- α collision process. The Ly- α volume production
219 rate was derived from the saved positions of Ly- α processes by collecting the number of the Ly-
220 α collision processes at a given altitude range. Then the Ly- α volume emission was derived by
221 using a 1-D approximation, *i.e.*, assuming that the area of the emission perpendicular to the x-
222 axis is equal to the initial area in the solar wind through which the precipitating particles initially
223 came. In the plots presented in this paper the Ly- α emission altitude profiles were derived in 1
224 km altitude bins.

225 2.2.1.3. *Bisikalo/Shematovich et al. 1-D Monte Carlo model*

226 The Bisikalo/Shematovich *et al.* model is a 1-D Monte Carlo model. The model considers
227 three primary processes: 1) precipitation of high-energy hydrogen atoms and protons that lose
228 their kinetic energy in the elastic and inelastic collisions, 2) ionization of target atmospheric
229 molecules/atoms, and 3) charge transfer and electron capture collisions with the major
230 atmospheric constituents (*i.e.*, CO₂, N₂, and O). Secondary fast hydrogen atoms and protons carry
231 enough kinetic energy to cycle through the collisional channels mentioned above and result in a
232 growing set of translationally and internally excited atmospheric atoms and/or molecules.

233 To study the precipitation of high-energy H/H⁺ flux into the planetary atmosphere, we use
234 the kinetic Monte Carlo model to solve the kinetic Boltzmann equations (Shematovich *et al.*,
235 2011; Gérard *et al.*, 2000) for H⁺ and H. The model is 1-D in geometric space and 3-D in
236 velocity space. Nevertheless, the 3-D trajectories of H/H⁺ are calculated in the code with final
237 projection on radial direction. The current version of the MC model (Shematovich *et al.*, 2019)
238 incorporates the full structure of the induced magnetic field of Mars; that is, all three components
239 of the magnetic field $\mathbf{B} = \{B_x, B_y, B_z\}$ are taken into account. The details of the model
240 implementation and statistics control with the variance below 10% can be found in Shematovich
241 *et al.* (2019).

242 The essence of the kinetic Monte Carlo model is accounting of all possible collisions in
243 the atmospheric region studied. Therefore, statistics for all collisional processes are accumulated

244 during the numerical realization of the kinetic model of the proton aurora. It provides a good
245 basis for the evaluation of the Ly- α source functions as keeping all excitation processes and their
246 spatial characteristics makes it possible to determine the statistical distribution of the emitted Ly-
247 α photons.

248 A key aspect of this model is the probabilistic treatment of the scattering angle distribution,
249 which influences both the energy degradation rate and the angular redistribution of the
250 precipitating protons and hydrogen atoms (Bisikalo *et al.*, 2018; Shematovich *et al.*, 2019). The
251 model utilizes both total and differential cross sections when calculating the post-collision
252 velocities for high-energy precipitating H/H⁺ and atmospheric particles.

253 The region under study is limited by the lower boundary, which is placed at 80 km, where
254 H/H⁺ particles are efficiently thermalized. The upper boundary is set at 500 km, where
255 measurements or calculations of the precipitating fluxes of protons or hydrogen atoms are used
256 as a boundary condition. Both table and/or analytic (Maxwellian and/or kappa-distribution)
257 functions representing the energy spectra as well as the pitch-angle (monodirectional, isotropic,
258 or limited by cone) distributions of precipitating particles could be used at the upper boundary.

259 2.2.1.4. Gronoff *et al.* 1-D Kinetic model (“Aeroplanets”)

260 The Gronoff *et al.* model, called Aeroplanets, utilizes a 1-D Kinetic transport approach.
261 Aeroplanets (Gronoff *et al.*, 2012a; Gronoff *et al.*, 2012b; Simon Wedlund *et al.*, 2011) is based
262 on an auroral particle precipitation model initially developed for the Earth and later adapted to
263 Mars (as well as numerous other planetary bodies, *e.g.*, Venus and Titan). This model computes
264 the ionization and excitation of atmospheric species by photon, electron, proton, and cosmic ray
265 impacts, including the effect of secondary particles. The proton transport module within
266 Aeroplanets is based on the work of Galand *et al.* (1997 and 1998), Simon (2006), and Simon *et al.*
267 (2007) for Earth, who solved semi-analytically the coupled proton-hydrogen dissipative
268 kinetic transport equation for protons and hydrogen atoms charge-changing with neutral gas. It
269 was originally developed from the idea that dissipative forces responsible for angular
270 redistributions (due to elastic scattering) can be introduced in the force term of the general
271 dissipative Boltzmann equation (Galand *et al.*, 1997). As such, angular redistributions due to
272 magnetic mirroring effects and to collisions are naturally included, leading to backscattering.

273 Inputs to the Aeroplanets model include cross sections, the vertical profile of atmospheric
274 neutral densities (*i.e.*, composition at different altitudes), and the precipitating fluxes of particles
275 such as H and H⁺ at the top of the atmosphere (any shape and energy distribution can be
276 prescribed). Outputs include the vertical profile of H and H⁺ differential energy fluxes, and the
277 vertical profile of the production rate of excited and ionized species and electrons, including
278 emissions. Simulations are performed on a grid typically spanning 90 to 250 km (approximately,
279 the exobase level).

280 Cross sections in Aeroplanets are taken from the latest version of the ATMOCIAD
281 (Gronoff *et al.*, 2021) cross section and reaction rate database compiled and developed by Simon
282 Wedlund *et al.* (2011) and Gronoff *et al.* (2012a). In ATMOCIAD, experimental and theoretical
283 cross sections as well as their uncertainties are collected. Although ATMOCIAD is an extensive
284 collection of cross sections, we note that there is still a rather poor characterization of cross
285 sections at low energies (typically in the sub-keV range). Regarding differential cross sections,
286 Aeroplanets uses phase functions that are convolved with the energy-dependent cross sections
287 described above.

288 Aeroplanets is well qualified for the fast computation of the proton precipitation from a
289 measured spectra near the planet, and for the fast computation of the whole effect of that
290 precipitation thanks to its coupling with a secondary electron transport model. The analytic
291 computation approach prevents the computation within very complex magnetic topologies
292 (which are best handled by Monte-Carlo models) but is suited for handling large sets of initial
293 angles and energies.

294 2.2.2. Radiative Transfer Model

295 To quantitatively compare the proton aurora modeling results and the IUVS limb
296 observations it is necessary to perform a radiative transport calculation (done in this study using
297 a Radiative Transfer model created by coauthor Deighan). While the Ly- α emission from thermal
298 hydrogen is optically thick in the upper atmosphere of Mars (Anderson and Hord, 1971), the
299 emission associated with proton aurora can be considered optically thin due the large Doppler
300 shifting caused by the high velocity of the ENAs (Gérard et al., 2019). This both offsets the line
301 center and broadens the width of the spectral line shape and ensures that few of the photons
302 produced by proton aurora interact with the ambient thermal hydrogen population for most
303 viewing geometries. This allows a simple line-of-sight integration to be employed, though CO₂
304 absorption must still be taken into account (Deighan *et al.*, 2018; Gérard *et al.*, 2019).

305 The procedure used to calculate a model brightness to compare with each measurement
306 by IUVS is as follows: First, the model atmosphere is sampled at 1 km intervals starting from the
307 reconstructed spacecraft position and extending out 3000 km along the line-of-sight vector. This
308 ensures adequate sampling of the model volume emission rate (VER), as the auroral emission
309 typically has a scale height on the order of 10 km and a peak VER occurring 500-1700 km away
310 from the spacecraft for IUVS periapsis limb scans. The column of CO₂ between the spacecraft
311 and each sample point in the model is then integrated and an absorption optical depth is
312 obtained using an absorption cross section of 7.348×10^{-20} cm² (Huestis and Berkowitz, 2010).
313 The Beer-Lambert law is then applied to find the attenuation caused by CO₂ absorption for each
314 sample point and the attenuated VER is integrated to obtain a column emission rate (CER). This
315 is readily converted into the brightness unit of Rayleighs (R) conventionally used for airglow and
316 aurora (Hunten *et al.*, 1956). The proton aurora VER and CO₂ densities are both assumed to have
317 spherical symmetry (primarily driven by the use of 1-D profiles), and the brightness calculation
318 itself is performed using an integration through 3-D space along each line of sight.

319 3. Inputs and Results for Inter-model Comparison (Step 1)

320 3.1. Purpose and Description of Step 1

321 We begin the campaign with an inter-model comparison in Step 1 using multiple
322 different test cases of representative inputs to represent varying proton aurora conditions. The
323 purpose of this step is to set a baseline for inter-model comparisons, and to compare the effects
324 of varying input conditions on the results of each individual model.

325 We use five different representative proton aurora conditions, each with varying solar
326 wind velocity, H-ENA and proton fluxes at the top of the atmosphere, and CO₂ density profiles
327 for high and low atmospheric temperature conditions (Table 1). Using these inputs, altitude
328 versus Ly- α volume emission rate profiles were created by each model for each representative
329 test case. In Step 1-A, we first compare the results in each modeler's native format (*e.g.*, volume

330 emission rate). In Step 1-B the results are forward-modeled into observation space using the
331 radiative transfer model. In Section 5 we discuss possible causes for the observed inter-model
332 discrepancies.

333 3.2. Assumptions/Constraints for Step 1

334 To accurately compare the driving physics incorporated in each of the models, we
335 implement a number of constraints on each model in Step 1 (*i.e.*, the inter-model comparison
336 step). The three primary constraints are 1) assuming the incident solar wind particle beam (either
337 purely H or purely H⁺) is monoenergetic; 2) assuming purely 1-D anti-sunward solar wind
338 particle movement (*i.e.*, monodirectional) incident at the subsolar point (*i.e.*, SZA = 0°); and 3)
339 requiring that the same cross section processes be included in each model (yet allowing the use
340 of different cross section values; see Section 5.1 and Supplementary Table S1 for more details).
341 We empirically justify inclusion of the first two constraints based on previous observations of
342 penetrating protons showing a monoenergetic population (*i.e.*, typically the same energy as the
343 solar wind) that is incident across the entire sunward-facing side of the planet (*e.g.*, Halekas *et al.*,
344 2015). For the third constraint, we specifically consider five cross section processes for
345 protons and/or H interacting with CO₂: elastic, charge exchange/electron capture, electron
346 stripping, ionization, and Ly- α . Although all models have the ability to incorporate additional
347 processes (see Supplementary Table S1), most have incorporated exclusively these five
348 processes. We note that the Bisikalo/Shematovich *et al.* team also included cross section
349 processes for Hydrogen Balmer-alpha and -beta; however, this inclusion produces only a very
350 minor effect on the resulting volume emission rate (VER) due to the relatively small cross
351 sections of these processes. Each modeling team also incorporated their own DSCS values
352 (Supplementary Table S1). Lastly, while the Jolitz and Kallio models use similar 1 km linear
353 altitude bins, the other two models utilize different types of altitude binning (we note however,
354 that a comparison of the type and spatial resolution of the altitude bins used by the Gronoff *et al.*
355 model found that this parameter to have a negligible effect on the simulation results).

356 3.3. Representative inputs for Step 1

357 In undertaking the inter-model comparison, we create five representative proton aurora
358 events to be simulated by each model (Table 1). We select baseline cases that resemble previous
359 observations of the particle flux, velocity, and neutral CO₂ temperature of Martian proton aurora
360 (*e.g.*, Deighan *et al.*, 2018), and incrementally change the input parameters in each case in order
361 to quantify the effect of the parameters on the proton aurora profile. In the two baseline cases we
362 vary the type of incident particle at the top of the model atmosphere (*i.e.*, 100% H-ENAs or
363 100% protons in Case 1 and Case 2, respectively); in subsequent cases we vary the average
364 incident particle beam flux (Case 3), the particle velocity (Case 4), and the neutral atmospheric
365 temperature (Case 5). By changing the temperature in Case 5, we also modify the scale height,
366 and thereby the CO₂ density profile. In Step 1 we do not include any representative cases that
367 consider variability associated with magnetic fields or solar zenith angles (SZAs) (*i.e.*, the
368 models simulate particle incidence at the subsolar point, where the Ly- α intensities are highest on
369 the planet). While these constraints are not necessarily indicative of the actual Mars-solar wind
370 interactions, they represent simplified scenarios that are beneficial for gauging inter-model
371 variability. We note that in this study we are exclusively interested in modeling the proton aurora
372 profile under different input conditions; since proton aurora are almost entirely formed due to
373 interactions between the incident particles and the neutral CO₂ atmosphere, the model results do

374 not directly incorporate processes occurring in the extended corona upstream of the bow shock
 375 (e.g., charge exchange between solar wind protons and the H corona; however, all but Case 2
 376 implicitly include this process).

377 *Table 1: Representative input for the five example cases in the inter-model comparison step (Step 1). These parameters were*
 378 *varied to assess their relative importance in each model.*

	Case 1 (Baseline w/ H-ENAs)	Case 2 (Baseline w/ Protons)	Case 3 (Small Flux)	Case 4 (High Velocity)	Case 5 (Hot Atmosphere)
v [km/s]	400	400	400	800	400
$F_{\text{H-ENA}}$ [$\text{cm}^{-2}\text{s}^{-1}$]	10^7	0	10^6	10^7	10^7
F_{proton} [$\text{cm}^{-2}\text{s}^{-1}$]	0	10^7	0	0	0
CO ₂ Density Profile (varying Temp)	CO ₂ profile @ T=190K	CO ₂ profile @ T=240K			

379

380 In order to vary the neutral atmospheric temperature parameter in the models (Case 5) we
 381 create two different CO₂ density profiles, each containing altitude-binned (1 km bin)
 382 representative CO₂ number density values for the two respective temperature ranges of 190 K
 383 (i.e., baseline temperature) and 240 K (i.e., high temperature). These different CO₂ density
 384 values were created using a standard barometric isothermal atmosphere described by the
 385 equation:

386

$$n(z) = n_{\text{ref}} \exp(- (z - z_{\text{ref}}) / H), \quad (1)$$

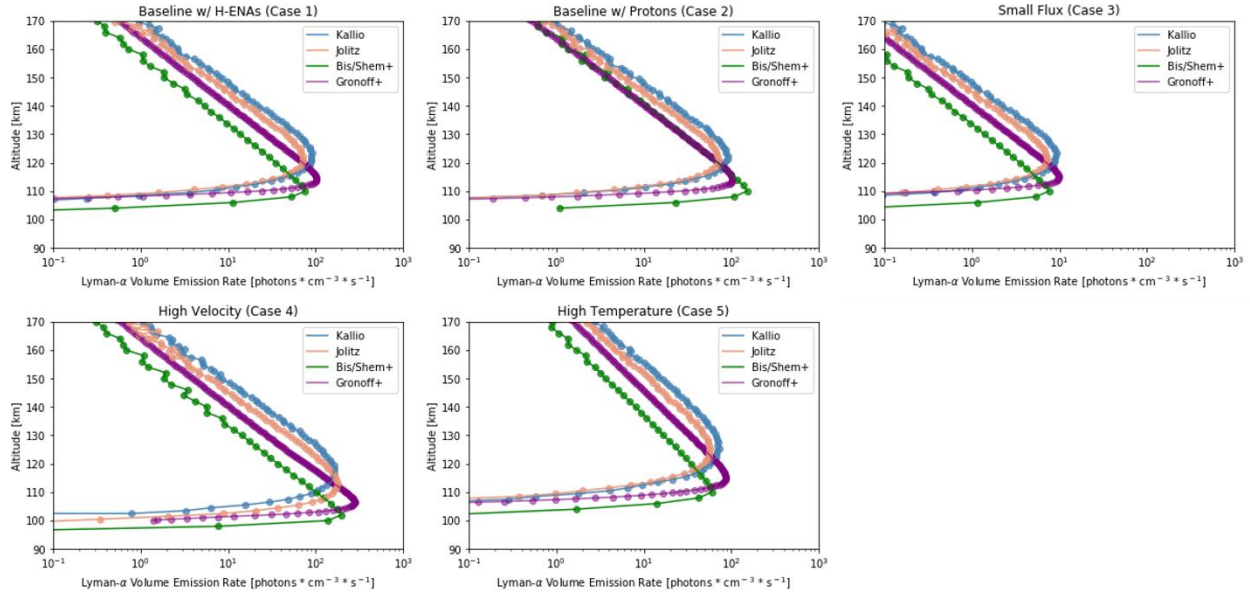
387 where z is altitude, n_{ref} is the number density at a reference altitude, z_{ref} is the chosen reference
 388 altitude (in this case, 120 km), and H is the CO₂ scale height. Here we assume $n_{\text{ref}} = 1 \times 10^{11} \text{ cm}^{-3}$
 389 at 120 km, and H is calculated for each temperature range using a value of $g = 3.46 \text{ m/s}^2$ (i.e., g
 390 at the reference altitude of 120 km). The calculated scale height values for the low and high
 391 temperature cases were 10.4 km and 13.1 km, respectively.

392

3.4. Results of Step 1-A

393 The results of the inter-model comparison in Figure 1 show many similarities between
 394 the different modeled proton aurora volume emission rates (VERs), with the results of the Jolitz
 395 and Kallio models exhibiting the most similarities. Interestingly, most models predict similar
 396 trends in the relative changes observed between each of the five representative cases. There is a
 397 large range in the proton aurora peak altitudes between the models, with the
 398 Bisikalo/Shematovich *et al.* model consistently predicting the lowest peak altitudes and the
 399 Gronoff *et al.* model predicting the second lowest. The peak altitudes in the Jolitz and Kallio
 400 models are consistent with each other in nearly every case, with the exception of the high
 401 velocity case (Case 4), where the Jolitz model predicts a slightly lower peak altitude than the

402 Kallio model. The Gronoff *et al.* model also consistently predicts the largest peak VERs in each
 403 case (with the exception of Case 2, where the Bisikalo/Shematovich *et al.* model predicts the
 404 largest peak VERs). Almost all of the models show no difference in the proton aurora profile
 405 (*i.e.*, VER or altitude) based on varying the type of incident particle at the top of the atmosphere
 406 (*i.e.*, H-ENA or proton; compare Case 1 and Case 2 profiles); the only exception being the
 407 Bisikalo/Shematovich *et al.* model, which predicts a slight increase in the VER of the proton
 408 aurora profile for protons rather than H-ENAs as the incident particle. The similarities between
 409 Cases 1 and 2 suggest that most models do not predict significant differences between a H-
 410 induced Ly- α emission and a proton-induced Ly- α emission in the proton aurora profile.



411

412 *Figure 1: Simulated Ly- α volume emission rates of proton aurora at different altitudes from each model in this study for the five*
 413 *representative input cases in the inter-model comparison step of the campaign (Step 1-A). The two input parameters that have the*
 414 *most significant effect on the results are the incident solar wind flux and velocity. See Table 1 for the input parameters used in*
 415 *each of the five representative cases.*

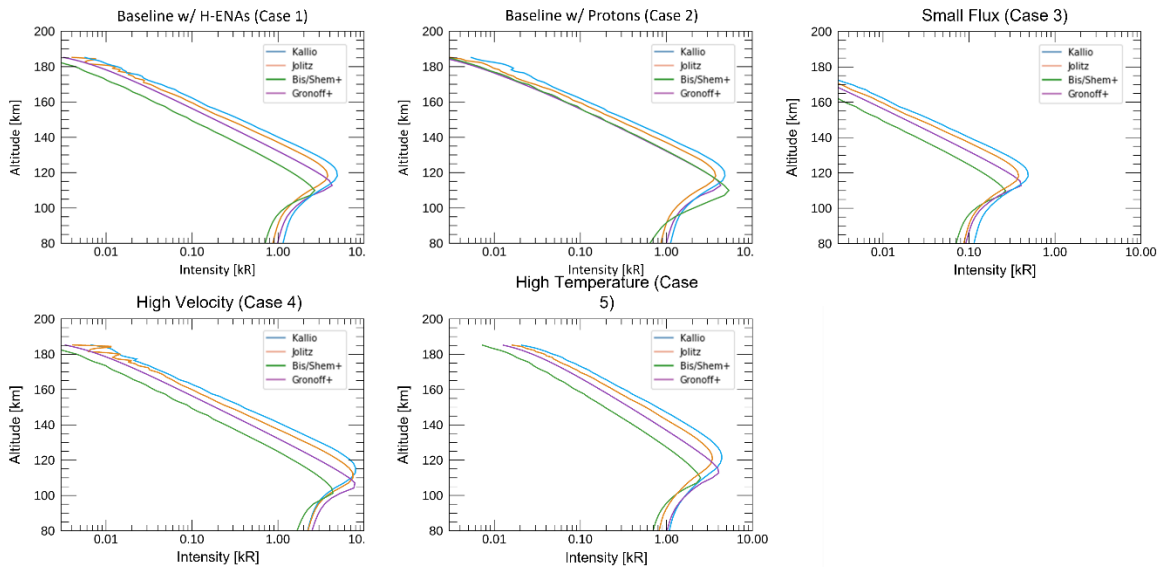
416 3.5. Results of Step 1-B

417 In Step 1-B we forward-model the results of Step 1-A into observation space (*e.g.*,
 418 perform a “line-of-sight” integration comparison). In this step we produce synthetic observations
 419 that would be made by MAVEN/IUVS given the computed volume emission rates. In so doing,
 420 the model results are converted from Ly- α volume emission rate (in units of photons/cm³s) to
 421 Ly- α intensity (in units of kilorayleighs, kR) using the previously described radiative transfer
 422 model. Using the same radiative transfer model to forward-model each simulation’s output in
 423 this step enables a more reliable cross-model comparison.

424 As shown in Figure 2, the results of Step 1-B further reveal similarities in the model
 425 intensities and peak altitudes for each of the five cases. We find consistently in each model that
 426 the two major variables that affect the proton aurora profile are the penetrating particle flux and
 427 the particle velocity. Decreasing the flux by an order of magnitude (Case 3) correspondingly
 428 decreases the Ly- α intensity by an order of magnitude. Similarly, doubling the particle velocity
 429 (Case 4) noticeably increases the peak intensity in each model and decreases the peak altitude by
 430 ~5-10 km. In the final representative input case of increasing the atmospheric temperature

431 (thereby changing the neutral atmospheric scale height) (Case 5), all of the models show a slight
 432 decrease in the Ly- α peak intensity and a change in the shape of the profile at higher altitudes
 433 (*i.e.*, the profile has a broader shape). Additionally, most of the models show an increase in the
 434 peak altitude by \sim 1-5 km in Case 5 (with the exception of the Bisikalo/Shematovich *et al.* model,
 435 which does not exhibit a change in the peak altitude due to the changing temperature/scale
 436 height). The differences in the profile observed in Case 5 are likely present because the volume
 437 emission rate, and therefore the unattenuated auroral brightness, scales inversely with the
 438 atmospheric scale height in order to conserve photon production in the atmosphere; this in turn
 439 causes the Ly- α brightness to appear more “spread out” across different altitudes in the proton
 440 aurora profile.

441 The consistency of these results between models confirms our understanding of the
 442 driving processes that have the most significant effect on the proton aurora profile. Particularly,
 443 we see in Cases 3 and 4 that the solar wind proton velocity and density (which also affect the
 444 particle energy and flux) are tremendously important in the formation of notable proton aurora
 445 events. Thus, we may extrapolate from the results that high velocity and/or density solar events
 446 (*e.g.*, coronal mass ejections and corotating interaction regions) will correspondingly create
 447 significantly enhanced proton aurora events. This finding is consistent with preliminary studies
 448 of proton aurora at Mars in which the observations were found to correspond with extreme solar
 449 activity events (*e.g.*, Ritter *et al.*, 2018).



450
 451 *Figure 2: Simulated Ly- α intensities from the inter-model comparison after running the results of Step 1-A through the radiative*
 452 *transfer (RT) model (Step 1-B), which forward-models the results into observation space (*e.g.*, performs a “line-of-sight”*
 453 *integration comparison). The model results more closely resemble each other after this step, but the dominant influencing factors*
 454 *identified in Step 1-A (Figure 1) are still present. See Table 1 for the input parameters used in each of the five representative*
 455 *cases.*

456 4. Inputs and Results for Data-Model comparison (Step 2)

457 4.1. Purpose and Description of Step 2

458 In the second step, we assess the robustness of each of the models based on their abilities
 459 to reproduce a typical proton aurora detection from the MAVEN/IUVS dataset. In undertaking

460 Step 2, different variables in the models were tuned to match proton aurora events in the
461 MAVEN/IUVS dataset. The models use relevant data inputs for a specific proton aurora event to
462 attempt to accurately reproduce the event. As in Step 1, the model results in Step 2-A are first
463 provided in their native formats, and subsequently forward-modeled into observation space in
464 Step 2-B using the radiative transfer model.

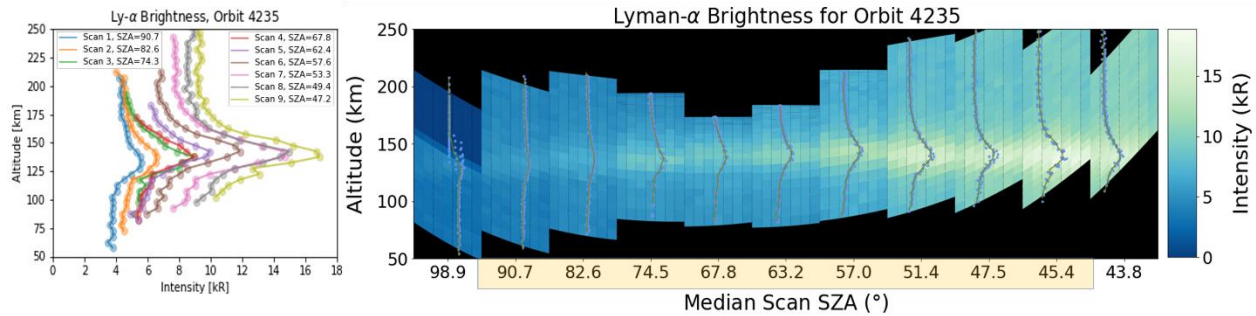
465 4.2. Description of Example Proton Aurora Event and MAVEN/IUVS Observations

466 For the data-model comparison stage of the campaign (Step 2), we selected an example
467 of a proton aurora event from the MAVEN/IUVS dataset that occurred during the periapsis
468 portion of MAVEN orbit #4235 (*i.e.*, December 3rd, 2016, starting at ~13:44 UTC). This
469 particular proton aurora event occurred at relatively low SZAs around southern summer solstice
470 ($L_s \sim 270^\circ$), a period of time exhibiting frequent proton aurora activity and increased dust activity
471 associated with the concurrent Martian dust storm season. Figure 3 shows the IUVS Ly- α
472 intensity data for this orbit. The left-hand plot of Figure 3 shows the Level 1C altitude-binned
473 Ly- α altitude-intensity profiles for each of the limb scans used in the study; and the right-hand
474 plot shows these profiles overlain on a synthetic image format of each of the IUVS limb scans
475 from this orbit (horizontal), showing the Ly- α intensity for each of the 21 IUVS mirror
476 integrations (vertical) and 7 spatial bins within each scan (*e.g.*, similar to Figure 2 in Deighan *et*
477 *al.*, 2018). Note that the scans are displayed as though they are contiguous even though
478 spacecraft and slit motions prevent full spatial coverage. There are eleven IUVS limb scans in
479 this orbit, but we use only the middle nine IUVS scans in this study (yellow highlighted scans in
480 Figure 3). In evaluating the robustness of each of the models in this step of the study, the model
481 results were compared with intensities and peak altitudes of the IUVS Ly- α profiles from these
482 nine scans.

483 There are minor peak altitude variations in IUVS Ly- α observations between scans
484 throughout this orbit. These minor altitude variations correspond with similar altitude variations
485 in the IUVS CO₂⁺ ultraviolet doublet emission (CO₂⁺ B 2 Σ \rightarrow X 2 Σ around 288 nm) (not
486 shown), suggesting the possible presence of waves and/or tides in the neutral atmosphere during
487 this orbit (*e.g.*, Lo *et al.*, 2015; England *et al.*, 2016). The likely presence of waves/tides in this
488 orbit is strengthened by similar observations in the MAVEN/NGIMS inbound CO₂ altitude-
489 density profile. We note, however, that altitude variations in the Ly- α and CO₂⁺ emissions are
490 less than 5 km, approaching the resolution limit of the observation; thus, the minor altitude
491 variations observed in the Ly- α peak intensity or CO₂ density during this orbit should not have
492 any significant influence on the modeled proton aurora profiles.

493 This particular proton aurora event exhibits an especially high orbit-mean Ly- α peak
494 intensity and emission enhancement (11.4 and 3.93 kR, respectively) as observed by IUVS. Also
495 notable during this orbit is a particularly high penetrating proton flux ($2.73 \times 10^6 \text{ cm}^{-2} \text{ s}^{-1}$)
496 observed by MAVEN's Solar Wind Ion Analyzer (SWIA) instrument (Halekas *et al.*, 2013).
497 SWIA observed a strong solar wind stream interaction during this orbit, resulting in this
498 especially high penetrating proton flux. The MAVEN periapsis during this orbit was in the
499 southern hemisphere on the dayside of the planet (with the exception of a few limb scan
500 observations near the terminator) (see Supplementary Figure S1 and Figure S2). Because the
501 spacecraft periapsis does not occur near any remanent crustal fields (Supplementary Figure S1),
502 we do not expect a significant influence (if any) from crustal fields during these observations.

503 The average upstream interplanetary magnetic field (IMF) magnitude and cone angle (*i.e.*, angle
504 off of the Mars-Sun line) during this orbit is ~ 10 nT and $\sim 45^\circ$, respectively.



505
506 *Figure 3: IUVS Ly- α intensity data of proton aurora observation used in the data-model portion of the campaign (Step 2). Left:*
507 *IUVS Level 1C altitude-intensity profiles for limb scans used in the study (MAVEN orbit #4235); SZA at the profile peak for each*
508 *limb scan is shown in the legend. Right: Altitude-intensity profiles overlain on top of a synthetic image format of Ly- α intensities*
509 *for each IUVS limb scan/mirror angle in this orbit (e.g., similar to Figure 2 from Deighan et al. 2018; see text for more details).*
510 *Note that the scans are displayed as though they are contiguous but spacecraft and slit motions prevent full coverage. Only the*
511 *central nine scans are used in this study (scans that are highlighted yellow at the bottom), and the SZA values shown at the*
512 *bottom correspond with the median SZA for each limb scan in the orbit.*

513 4.3. Background Subtraction of Coronal H Contribution from IUVS Ly- α Brightness

514 The Ly- α brightness observed in the IUVS data is created by contributions from not only
515 the non-thermal solar wind-derived H that produces proton aurora, but also from the thermalized
516 background coronal H. Thus, by subtracting out the background coronal H from the IUVS proton
517 aurora profiles, we are able to accurately compare the data with the model results. We perform
518 this coronal H background subtraction by first estimating the background coronal H brightness
519 during this time using IUVS limb scan profiles from a nearby orbit that exhibits little/less
520 evidence of enhancement due to proton aurora activity at a similar SZA (in this case we use orbit
521 #4229, as it exhibits the least contribution from proton aurora than any surrounding orbits).
522 These heuristic coronal Ly- α profiles are created by fitting an arcsine function to the upper- and
523 lower-most altitudes of the Ly- α profiles from the nearby orbit with little/less proton aurora
524 activity. Each heuristic profile of the estimated background Ly- α brightness due to the coronal H
525 in a given orbit is then subtracted out from each corresponding IUVS limb scan at a similar SZA
526 from the orbit of interest containing strong evidence of proton aurora (see Supplementary Figure
527 S3 for Ly- α profiles before and after background subtraction and heuristic coronal background
528 profiles used). This method is similar to the background subtraction methodology used by
529 Deighan *et al.* (2018) but differs in the determination of the background coronal H profile due
530 the absence of nearby orbits that completely lack proton aurora (*i.e.*, because of the before
531 mentioned near continuous proton aurora activity during the southern summer season). The
532 corrected intensities should then more closely reflect the H Ly- α contribution only from proton
533 aurora. In order to determine its effectiveness, this background coronal H subtraction technique
534 was tested on numerous other IUVS proton aurora detections and found to be a highly effective
535 empirical method for isolating the proton aurora contribution to the IUVS Ly- α observations.
536 However, as this methodology estimates a heuristic background coronal H by assuming
537 minimal/no changes in the neutral atmosphere between multiple orbits, there will be inaccuracies
538 in the corrected proton aurora profiles; we estimate these inaccuracies to be only a fraction of a
539 kR at most.

540 As shown in Supplementary Figure S3, the IUVS Ly- α intensities are reduced
 541 significantly due to this background-subtraction routine (by nearly 10 kR at low SZAs), but the
 542 shape of the profiles around the proton aurora profile peak (*i.e.*, between ~110-150 km) does not
 543 change. The profile peak altitudes typically also do not change as a result of this background
 544 subtraction methodology, provided that the peak altitudes of the proton aurora orbit profiles are
 545 not significantly different from those of the background subtraction orbit profiles (*i.e.*, the nearby
 546 orbit with little/less enhancement due to proton aurora). However, because of a slight difference
 547 in peak altitudes between the orbit considered in this study and the orbit used for the background
 548 subtraction routine (*i.e.*, orbits 4235 and 4229, respectively) at the lowest SZA profile, the peak
 549 altitude of the SZA ~45° background subtracted profile has been (artificially) slightly shifted
 550 down by ~5 km.

551 4.4. Assumptions/Constraints for Step 2

552 In Step 2, the models used inputs drawn from observations made by MAVEN (discussed
 553 more below). We apply many of the same constraints and assumptions as those applied in Step 1
 554 (*i.e.*, assuming a monoenergetic incident particle beam and monodirectional incident particle
 555 movement, and constraining the cross section processes used). One notable difference in Step 2
 556 is that the models produced outputs at a range of solar zenith angles (*i.e.*, not just at the subsolar
 557 point) in order to simulate the different SZAs of each of the IUVS limb scans in this orbit. As in
 558 Step 1, we exclude any effects due to electric or magnetic fields.

559 In order to additionally simplify the inputs for this step, all models assume that the
 560 incident particle population is composed entirely of H-ENAs at the top of the atmosphere (*i.e.*,
 561 assuming an initial penetrating proton component equal to zero). Based on our findings in Step 1,
 562 the proton aurora profile does not significantly change in most models when assuming 100%
 563 protons or 100% H-ENAs. Thus, this assumption of particle composition should not significantly
 564 affect the final results. The initial H-ENA flux ($F_{\text{H-ENA}}$) is approximated using the equation:

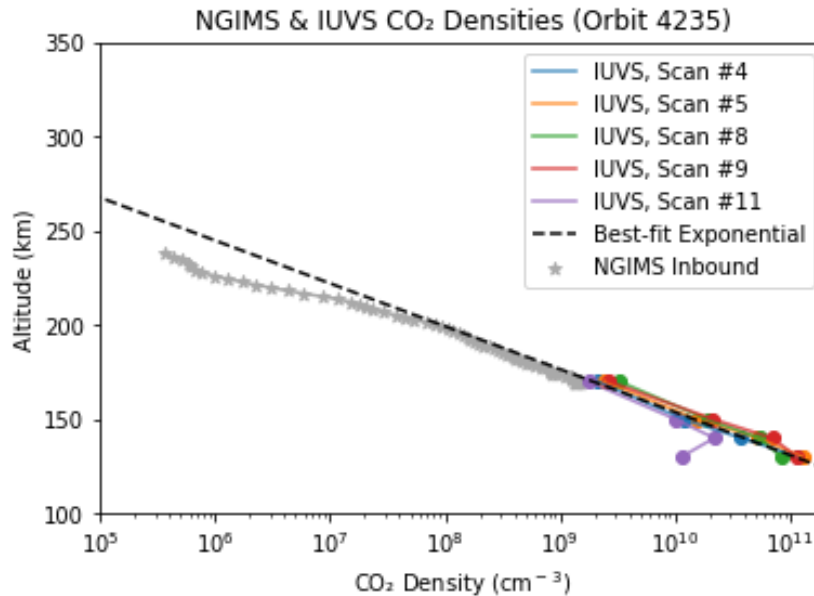
$$565 F_{\text{H-ENA}} = F_{\text{pp}} \times 13.5, \quad (2)$$

566 where F_{pp} (the orbit mean penetrating proton flux derived from SWIA) equals $2.73 \times 10^6 \text{ cm}^{-2} \text{ s}^{-1}$
 567 in this orbit, and 1/13.5 is the approximate fraction of the incoming beam of H-ENAs that is
 568 converted to protons. This conversion value was determined based on previous SWIA
 569 observations and the relevant energy-dependent electron stripping and charge exchange cross
 570 sections (*e.g.*, Halekas *et al.*, 2015; Halekas, 2017), assuming that at the point when H-H⁺
 571 equilibrium is reached in the collisional atmosphere (*i.e.*, the location of the SWIA measurement)
 572 the mix is ~92.5% ENAs and ~7.5% protons (*i.e.*, the equilibrium fractionation for the relevant
 573 cross sections at 1 keV).

574 Another constraint carried over from Step 1 is that all models used the same
 575 representative CO₂ density (*i.e.*, a 1 km altitude-binned CO₂ number density profile). However,
 576 in Step 2, the theoretical CO₂ density line profile is created based on neutral densities from two
 577 MAVEN instruments observing at different altitude ranges during this orbit: IUVS and the
 578 Neutral Gas and Ion Mass Spectrometer (NGIMS) (Mahaffy *et al.*, 2015). We note that although
 579 NGIMS data are acquired during both the inbound and outbound portions of the orbit, we restrict
 580 this study to include only inbound data, due to instrument artifacts which have been found to
 581 artificially increase CO₂ densities in NGIMS outbound data (*e.g.*, Stone *et al.*, 2018). The IUVS
 582 and NGIMS neutral densities are consistent with each other within the limited overlapping
 583 altitude range of the two instruments (*i.e.*, at a reference altitude of 170 km, the NGIMS CO₂

584 density is $\sim 1.48 \times 10^9 \text{ cm}^{-3}$, and the smallest derived CO_2 density from different IUVS limb
 585 scans is $\sim 1.74 \times 10^9 \text{ cm}^{-3}$).

586 Figure 4 shows the theoretical CO_2 profile for Step 2, which is created by fitting an
 587 exponential to the IUVS and inbound NGIMS data using equation (1). In this case, $n_{\text{ref}} =$
 588 $1.1 \times 10^{11} \text{ cm}^{-3}$ (the average IUVS density at reference altitude z_{ref}), $z_{\text{ref}} = 130 \text{ km}$ (the minimum
 589 altitude observed by IUVS during this orbit). The CO_2 scale height was estimated by varying the
 590 temperature value until an appropriate fit was achieved (using a value of $g = 3.41 \text{ m/s}^2$ at 130
 591 km); a temperature of 180 K was found for the best-fit line.



592
 593 Figure 4: Empirically-derived theoretical CO_2 profile used by models for the data-model comparison (Step 2). This profile was
 594 created by fitting a best-fit exponential to the derived IUVS and measured NGIMS inbound data from this MAVEN orbit.

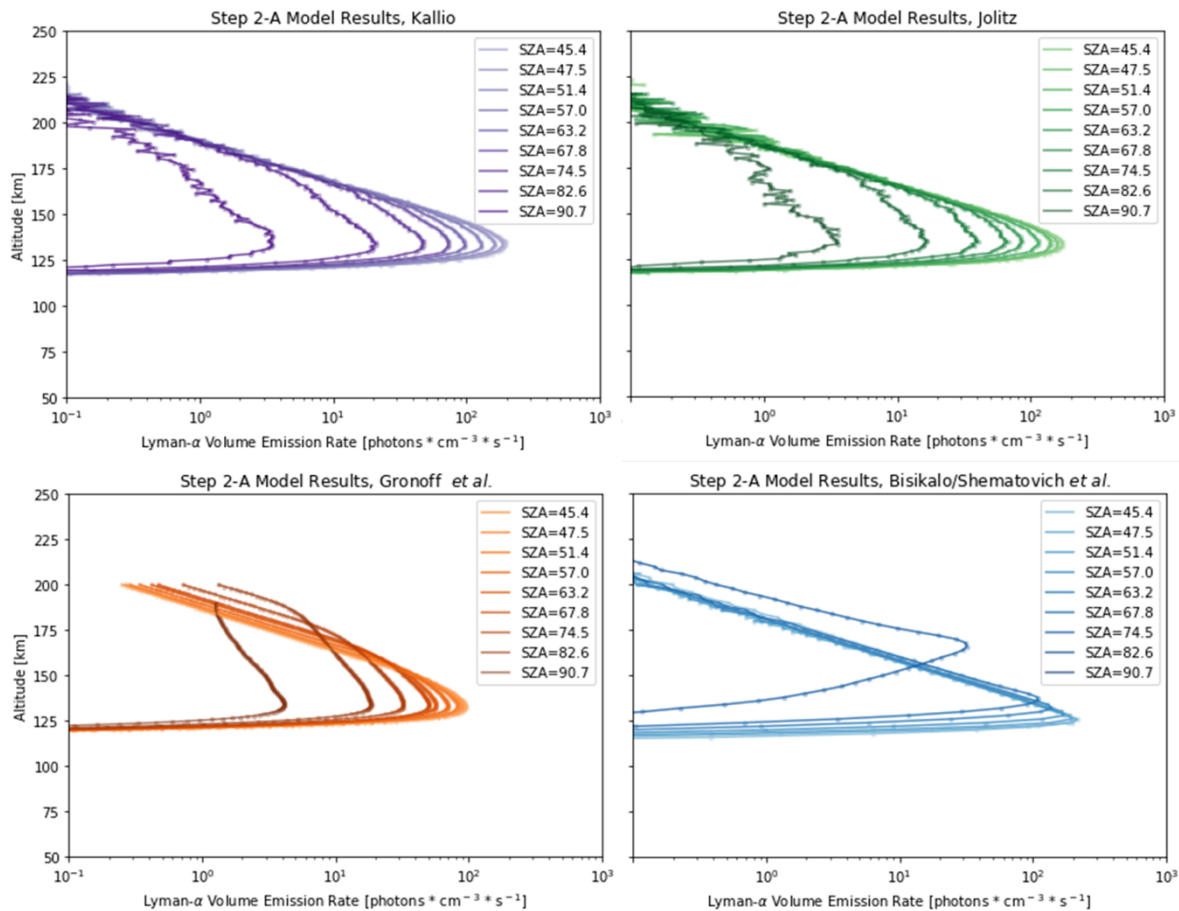
595 4.5. Results of Step 2-A

596 The results of Step 2-A show that all models simulate the input data to within less than an
 597 order of magnitude of the same volume emission rates (VERs) (Figure 5). As in Step 1, the
 598 results of Step 2-A also show that the Jolitz and Kallio simulations exhibit the most similarities
 599 to each other in terms of VERs and peak altitudes. The Gronoff *et al.* model results exhibit
 600 relatively low VERs compared with other models.

601 In Step 1, we used the models to simulate a proton aurora profile at a single SZA (*i.e.*, the
 602 subsolar point). However, in Step 2, each model simulated proton aurora profiles at numerous
 603 SZAs between $\sim 45^\circ$ - 90° . Thus, in Step 2 we are able to observe the decrease in Ly- α proton
 604 aurora brightness associated with increasing SZA. The proton aurora brightness appears to
 605 monotonically decrease in the Kallio, Jolitz, and Gronoff *et al.* simulations (particularly at low
 606 SZAs), but in the Bisikalo/Shematovich *et al.* simulation results the decrease is more gradual at
 607 lower SZAs (and pronounced at higher SZAs).

608 We note that the Bisikalo/Shematovich *et al.* Monte Carlo calculations for the two
 609 highest SZA profiles (*i.e.*, SZA= 82.6° and 90.7°) resulted in practically no Ly- α excitations
 610 (hence their absence on the plots in Figure 5 and Figure 6). The Bisikalo/Shematovich *et al.*

611 model results also exhibit relatively low peak altitudes at lower SZAs in comparison with other
 612 models; however, this model is the only one showing variability in the peak altitudes between
 613 SZA profiles. In this 1-D kinetic model, Ly- α photons are excited in local collisions of H-ENAs
 614 with the ambient atmospheric gas and the VERs are accumulated for the projection velocities of
 615 H-ENAs into the given SZA direction. In the case of high SZAs, the Ly- α excitations are caused
 616 mainly by the H-ENAs moving in the tangential trajectories relative to the upper atmosphere
 617 (*i.e.*, by H-ENAs which do not penetrate deep into the atmosphere). This results in: a) very low
 618 values of Ly- α VERs for high SZAs (especially for runs with SZA=82.6° and 90.7°); and b) an
 619 increase of the peak height of the profiles with SZA (*i.e.*, because the kinetic energy of collisions
 620 becomes lower for the excitation collisions along the tangential trajectories of the H-ENAs).



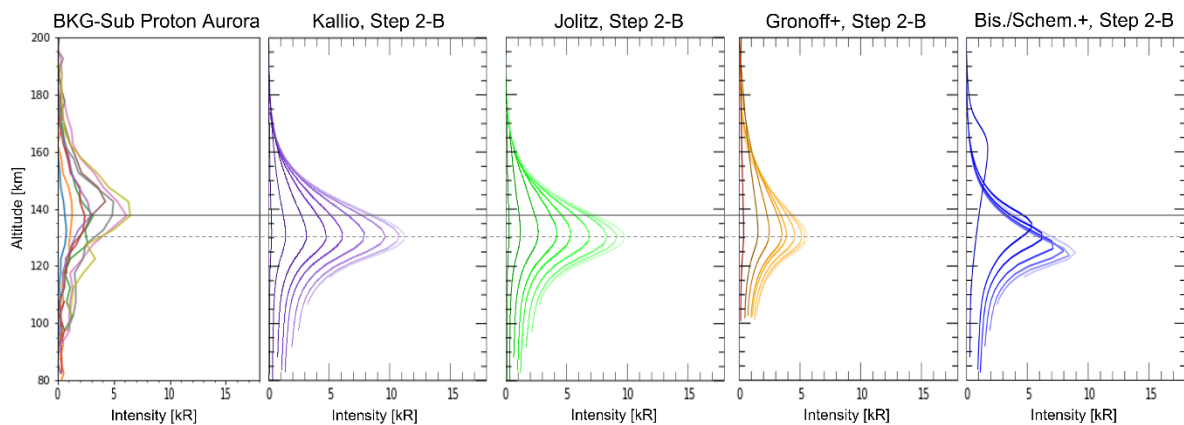
621
 622 *Figure 5: Simulation results from the data-model comparison step of the campaign (Step 2-A), showing proton aurora altitude-*
 623 *volume emission rate (VER) profiles from each model for the specified input parameters and SZAs. Most model results display*
 624 *similar peak altitudes and VERs agree with each other to within less than an order of magnitude. Note that SZA is decreasing*
 625 *from left-to-right between profiles in each panel.*

626 4.6. Results of Step 2-B

627 Forward-modeling the simulation results using the radiative transfer model in Step 2-B allows a
 628 more direct comparison between the model results and the IUVS data. In so doing, we find
 629 through Step 2-B that the models effectively reproduce the general shape of the data, with some
 630 models overestimating and some underestimating the proton aurora brightness (Figure 6). All of
 631 the peak altitudes from the model results are ~5-15 km lower than the observed peak altitudes.
 632 The simulated intensities of the Gronoff *et al.* and Bisikalo/Shematovich *et al.* model results for

633 the low SZA profiles (*i.e.*, profiles on the right-most side of each plot) are ~ 1 - 1.5 kR higher and
 634 lower (respectively) than the proton aurora intensities observed in the data for similar SZA
 635 profiles. However, at high SZAs, all three models for which profiles exist appear to simulate the
 636 data intensities effectively. The Kallio and Jolitz model intensities overestimate the data by a few
 637 kR at low SZAs, while the Gronoff *et al.* model intensities underestimate by a few kR. At low
 638 SZAs, the Bisikalo/Shematovich *et al.* model intensities closely correlate with the data
 639 intensities, but still slightly overestimate the data; however, the Bisikalo/Shematovich *et al.*
 640 intensities underestimate the data at high SZAs. While all models effectively simulate the shape
 641 and SZA variability of the data profiles, none of the model intensities match the data exactly
 642 (possible reasons for this discrepancy are discussed in the following section).

643 Significant peak altitude discrepancies between the models and the data are present in
 644 every model. This altitude discrepancy suggests that other processes/assumptions are not fully
 645 accounted for or understood in our evaluation of the results. In the following section, we
 646 examine numerous possible parameters that may contribute to the observed discrepancies
 647 between the data and the models.



648

649 *Figure 6: Simulation results for the data-model comparison after running the results through the radiative transfer model (Step*
 650 *2-B). The background-subtracted (*i.e.*, after subtracting out the theoretical “background” coronal H contribution) altitude-*
 651 *intensity profiles for this orbit are shown on the far left plot for comparison. The simulated proton aurora Ly- α intensities from*
 652 *each of the model results closely correlate with the data. However, note that there is still a discrepancy between the average peak*
 653 *altitude of the data profiles (solid grey horizontal line) and the average peak altitude of the model profiles (dashed grey*
 654 *horizontal line). Note also that the SZA of the observations is decreasing from left to right in all plots from SZA $\sim 90^\circ$ to SZA $\sim 45^\circ$*
 655 *(*i.e.*, moving toward the subsolar point), as shown in Figure 3 and Figure 5 legend.*

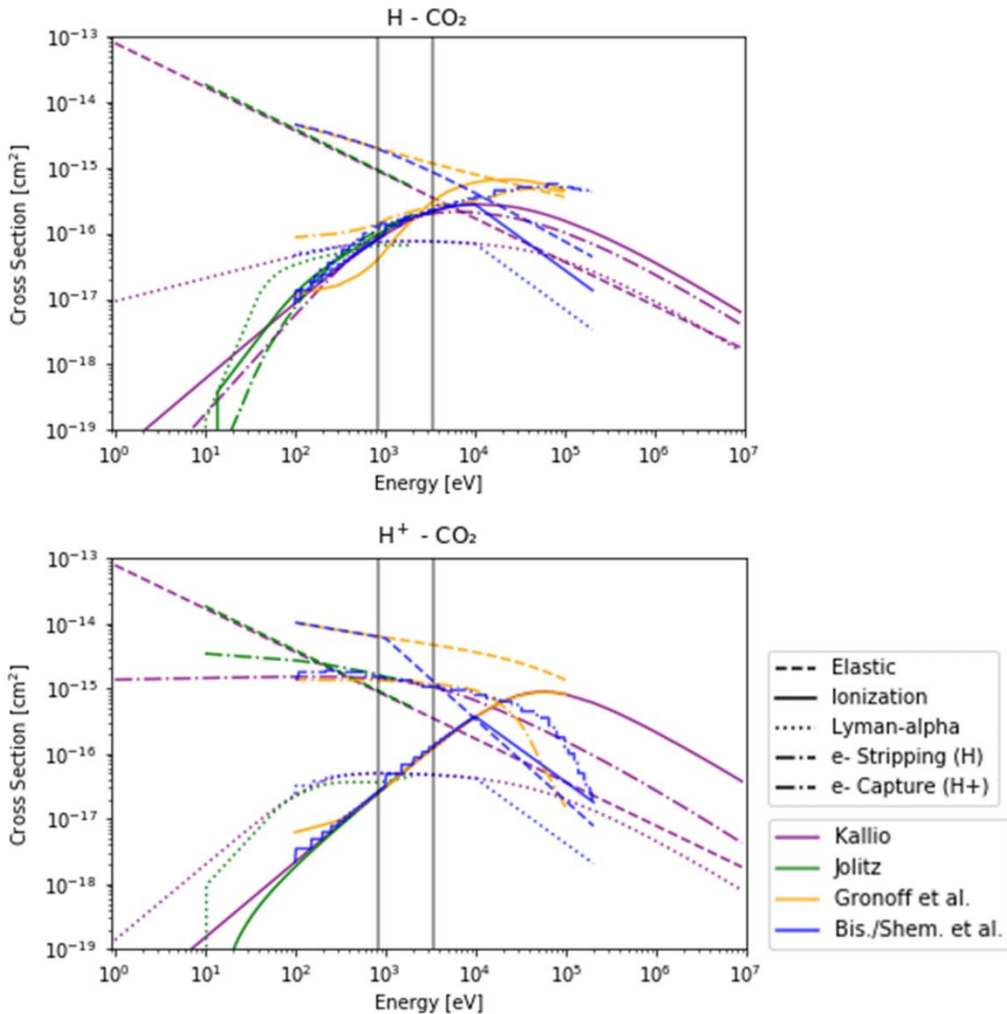
656 5. Discussion of parameters affecting model differences and data-model discrepancies

657 5.1. Cross Section Processes and Scattering Angle Distributions

658 Differences in cross section and DSCS values are a probable partial contributor to the
 659 differences in the results simulated by each model. While the models in this study utilize the
 660 same five processes, most models do not use the same cross sections (see Figure 7 and
 661 Supplementary Table S1 for details). As shown in Figure 7, these values can change significantly
 662 with varying energy ranges. The cross section values used in each model agree to within less
 663 than an order of magnitude of each other for the relevant energy range in this study (*i.e.*, 100 eV
 664 – 2 keV). The most variable cross section across the models were those used for elastic
 665 collisions, with elastic cross sections used by the Bisikalo/Shematovich *et al.* and Gronoff *et al.*
 666 models exceeding those used by the Kallio and Jolitz models by a factor of ~ 5 - 8 . These

667 differences can cause notable inter-model variability. Since many processes have not been
668 measured in a laboratory for proton/H collisions with CO₂, an interpolated or substitute value is
669 used for protons/H with O₂ or N₂. Particularly few measurements of protons with CO₂ are
670 available for Ly- α . Comparable cross section values are a likely cause for the similarities
671 observed between the Jolitz and Kallio results, and also a likely cause for the minor variability
672 between these two models in the data-model comparison (*i.e.*, the Jolitz model uses smaller Ly- α
673 cross sections at low energies and exhibits intensities that are 1-2 kR smaller than those of the
674 Kallio model at low SZAs).

675 Different implementations of scattering can also cause inter-model variations. A model
676 that assumes that a particle travels in the same direction before and after a collision (“forward
677 scattering”) will predict deeper particle penetration than a model that predicts variability in
678 scattering angle. Introducing even a small probability of non-forward scattering reduces the
679 precipitating flux and resulting emission rate. This is done by converting measured DSCS into a
680 phase function evaluated during a model run. In this study, each model uses different ways to
681 predict scattering (see supplementary material Text S1-S4 for detailed model descriptions).
682 Kallio and Jolitz use the same phase function to predict non-zero scattering angles after elastic
683 collisions, while all other collisions are assumed to be forward scattering. This, in tandem with
684 the same model approach (3-D Monte Carlo) likely contributes to their similar model
685 predictions. In contrast, the two 1-D kinetic Boltzmann solver models have slightly different
686 scattering models. Gronoff *et al.* uses a screened Rutherford phase function with a fixed
687 screening parameter in charge transfer and elastic collisions and assumes forward scattering in
688 ionization collisions. Bisikalo/Shematovich *et al.* uses the same assumptions for all collisions
689 except charge transfer, for which the model uses energy-dependent DSCS. The inclusion of non-
690 forward scattering in these 1-D models could be responsible for the lower intensities predicted by
691 these models compared to those predicted by the 3-D Monte Carlo models.



692
693
694
695
696

Figure 7: Available cross section values used by each modeling team (denoted by color) for the five different overlapping cross section processes considered in this study (denoted by line style). The solid vertical lines (grey) indicate the energy ranges evaluated in the representative cases in Step 1 assuming average (400 km/s) and high (800 km/s) solar wind velocities. See Supplementary Table S1 for more information regarding the cross section processes and relevant references in each model.

697 5.2. Data Quality and Caveats

698 In addition to the possible sources of discrepancy in the model assumptions, we must also
699 consider possible caveats associated with the datasets. Because IUVS is a remote sensing
700 instrument, its limb scan observations are created by integrating along the line of sight of the
701 instrument. However, the SWIA penetrating proton fluxes are measured *in situ* during periapsis,
702 and the orbit averaged value is used in this study. Because of the uniform nature of the processes
703 creating proton aurora across the dayside of the planet it is appropriate to combine these datasets;
704 nevertheless, there may be spatial and/or temporal discrepancies between these observations,
705 even though the data were acquired during the same MAVEN orbit.

706 Secondly, because IUVS Level 1C (L1C) data are processed and altitude-binned, we note
707 that minor discrepancies may be introduced in the Ly- α intensities during the data reduction
708 process. Calibrated IUVS L1C data are reported with a systematic uncertainty between ~ 10 -20%.
709 As the results of this study are sensitive to the absolute calibration of the instrument, we must

710 also consider any possible uncertainties in the IUVS reported intensities as a potential source of
711 discrepancy in the model-data comparison.

712 5.3. Other Assumptions

713 There are a number of additional assumptions in this study that may have led to
714 discrepancies between the models and the data. First, numerous data-driven assumptions are
715 made in creating the theoretical CO₂ density profile for Step 2. Any of three variables could be
716 altered that could in turn significantly affect the proton aurora profile: the energy of the incident
717 particles, the density of the atmosphere at the reference altitude, or the neutral atmospheric scale
718 height. All of these variables affect the peak altitude of the proton aurora profile, while changing
719 the scale height and energy also affects the profile peak intensity (more specifically, changing
720 the scale height can also affect how broad/narrow the profile shape becomes). Observations
721 made by MAVEN/SWIA during this orbit provide confidence that the calculation of particle
722 energy (based on average penetrating proton velocity) and the assumption of monoenergetic
723 particle behavior are appropriate/accurate, and therefore do not significantly affect the results.
724 However, in this study we determine the atmospheric density at the reference altitude (130 km)
725 by extrapolating from the average derived IUVS Level 2 CO₂ density at 130 km. Because the
726 spherically symmetric CO₂ density profile used by modelers in this study is theoretically derived,
727 inaccuracies in the assumed quantities for reference density or scale height would lead to an
728 inaccurate representation of the atmospheric density profile during this time. Thus, it is possible
729 that the CO₂ density profile is not entirely accurate in representing the atmosphere at this time,
730 possibly contributing to some of the discrepancies observed in the data-model comparison.
731 Moreover, only one neutral species (CO₂) is considered in our models, whereas other minor
732 species (*e.g.*, CO, O₂ and O) should also contribute to some extent to the observed profiles (in a
733 potentially important way, depending on altitude and latitude/longitude). Since H⁺/H cross
734 sections can vary significantly depending on the target neutral species (both in peak energy and
735 intensity), the modeling results presented may be modified further if these species are included.
736 We note, however, that because CO₂ is the overwhelmingly dominant species in the Martian
737 atmosphere, the inclusion of minor species should not alter any of the primary findings presented
738 in this study (but may decrease the observed discrepancies between the data and models). Such
739 an added complexity is outside the scope of the present study and a more in-depth investigation
740 of the inter-model's sensitivity to the neutral atmosphere composition is left for the future.

741 For simplicity in Step 2 we assume that the precipitating particle population at the top of
742 each model atmosphere is entirely composed of H-ENAs. Although the incident particle
743 population is indeed comprised of a fractionated portion of both ENAs and protons, this
744 simplified assumption is preferred over a non-empirical assumption of an estimated fractionation
745 ratio. Moreover, as the results in Step 1 do not significantly change in most models based on the
746 assumption of an entirely H-ENA- or proton-rich population, we would not expect the effects of
747 this assumption on its own to have a significant impact on the final results. One potential
748 exception may be for the Bisikalo/Shematovich *et al.* results in which the peak intensity
749 somewhat increases if a particle population of entirely protons is assumed (as seen in Step 1-A
750 and 1-B). Because the Bisikalo/Shematovich *et al.* results showed slight variability based on the
751 assumed incident particle population, it is possible that the intensities in their model results
752 might be larger if this assumption is changed (which may cause their simulated intensities to
753 more closely resemble those of the Kallio and Jolitz models, but to further overestimate the data
754 intensities in Step 2).

755 The chosen method for calculating the ENA flux may be a contributor to the observed
756 discrepancies between the data and model intensities. The H-ENA flux used in Step 2 is
757 calculated as an empirically derived multiple of the orbit-averaged SWIA penetrating proton
758 flux. While this ratio is supported by previous SWIA observations (*e.g.*, Halekas *et al.*, 2015;
759 Halekas, 2017), the value can vary based on seasonal or other changes (*e.g.*, the solar wind
760 proton flux, the neutral atmospheric scale height, or the location of the bow shock). As
761 determined in Step 1, decreasing the flux by an order of magnitude (which is the typical
762 variability observed throughout a Martian year, *e.g.*, Halekas, 2017) will correspondingly
763 decrease the proton aurora peak intensity by an order of magnitude. Thus, although the method
764 used to calculate the ENA flux is believed to be an accurate and statistically robust
765 approximation, any major deviation from the statistical norm of local conditions during this orbit
766 would cause discrepancies in accurately calculating the H-ENA flux.

767 Another possible contributor to the data-model discrepancies is the assumption of the
768 monodirectional movement of the incident particles in the atmosphere. We include a terminology
769 note here that in specifying “monodirectional” particle movement, we refer to the bulk velocity
770 (*i.e.*, average speed and direction) of the precipitating particles. All modeling teams represented
771 the incident precipitating particles as having a velocity fixed in magnitude (*e.g.*, 400 km/s and
772 800 km/s) and direction (anti-sunward). However, in reality the incident solar wind has nonzero
773 temperature, and has a broader variability than modeled. While some model teams investigated
774 the potential effects of this variability on the proton aurora profile (*e.g.*, Supplementary Figure
775 S4), the results are preliminary and will be reviewed in further detail in a future study.

776 In this study we do not consider the effects of electric or magnetic fields (*i.e.*, IMF,
777 induced, and/or crustal magnetic fields) on proton aurora. While most of the models do not
778 predict any likely significant change on the proton aurora profile caused by magnetic fields, a
779 previous modeling study by Gérard *et al.* (2019) (which utilized the Bisikalo/Shematovich *et al.*
780 proton/hydrogen precipitation model) predicted a decrease in the peak brightness of the proton
781 aurora profile in the presence of an induced magnetic field (*e.g.*, tens of nT). Comparatively, a
782 recent study by Henderson *et al.* (2022) that evaluated the effects of magnetic fields on
783 MAVEN/SWIA observations of penetrating protons suggests that only the very strongest
784 magnetic fields (*e.g.*, strengths greater than 200 nT) are expected to have a notable influence on
785 penetrating proton fluxes (*i.e.*, they did not find a significant influence for magnetic field
786 strengths on the order of 10 nT). Since the IMF magnitude during the MAVEN orbit included in
787 this study is non-negligible (*i.e.*, ~10 nT), it is possible that excluding magnetic/electric fields
788 from our study may contribute to some of the observed model-data discrepancies. However,
789 further analysis is required in order to understand the effects of magnetic fields (and variability
790 in field strengths) on the proton aurora profile.

791 Lastly, we also do not consider the effects of particle backscattering on the results of this
792 study. Because recent SWIA studies have shown that a significant portion of the incident particle
793 population can be backscattered (Girazian and Halekas, 2021), this factor could thereby
794 contribute to the data-model discrepancies (*e.g.*, potentially causing a lower observed proton
795 aurora brightness in the data than what is predicted by models). However, determining the
796 relative abundances of the forward- and back-scattered particle populations is outside the
797 purview of this study and thus the potential impacts on model results are not quantified herein.

798 5.4. Unique model Capabilities and Insights

799 As previously stated, the purpose of this campaign is not to identify the best or most
800 accurate model in the study, but rather, to characterize the ways in which each of the models
801 uniquely excel. In this section we identify aspects of each model that make them distinctively
802 capable in simulating proton aurora observations, as well as reasons for strong
803 agreement/disagreement between the models.

804 A few important aspects to consider are the cross sections used in each model, the
805 differences in the way the 3-D and 1-D solvers work, and how the relevant physics is treated.
806 The Monte Carlo solving techniques (*e.g.*, collision by collision determinators) and cross
807 sections used in the Kallio and Jolitz models are very similar (*e.g.*, Figure 7 and Supplementary
808 Table S1), leading to the observed similarities in their model results. In contrast to these two
809 models, the Bisikalo/Shematovich *et al.* and Gronoff *et al.* models generate outputs by solving
810 coupled proton-hydrogen kinetic Boltzmann transport equations. The Bisikalo/Shematovich *et al.*
811 model, which also uses Monte Carlo solving techniques, likely exhibits different results than
812 the former two models because of the use of different cross sections and 1-D model
813 dimensionality. The Gronoff *et al.* kinetic transport model uses cross section values different
814 than those of other models and a unique 1-D multistream kinetic transport solver. Nevertheless,
815 considering the variety of assumptions and technical implementations included in each model, it
816 is striking how well all of the models agree with each other as well as with the data.

817 The Bisikalo/Shematovich *et al.* model is the only one to simulate results that display
818 variability with SZA in the profile peak altitude: at low SZAs their simulated peak altitudes are
819 the furthest from the data peak altitudes, but at some higher SZAs their simulated peak altitudes
820 are closest to those of the data out of all models. Their model is unique in its incorporation of the
821 physics associated with this variability. However, we note that the peak altitudes simulated by
822 their model at very high SZAs are considerably higher than those typically observed for proton
823 aurora (*e.g.*, Hughes *et al.*, 2019).

824 The differences between the model results in the data-model comparison step
825 demonstrate the capabilities, assumptions, and methodologies of each of the models. The
826 Gronoff *et al.* and Bisikalo/Shematovich *et al.* models seem to be especially apt at approximating
827 the data intensities at lower SZAs (although the Bisikalo/Shematovich *et al.* simulated intensities
828 diverge the most at high SZAs). All models predict results which appropriately represent the
829 decrease in Ly- α brightness with increasing SZA: the Kallio, Jolitz, and Gronoff *et al.* models
830 appear to most accurately simulate this intensity falloff. The Bisikalo/Shematovich *et al.* model
831 appears to be particularly efficient at simulating the relative intensity differences between
832 profiles at lower SZAs, but the Jolitz model appears to be most consistently efficient across all
833 SZAs. While all models are effective at simulating the data, none of the four particle
834 precipitation models - which results are then run through the radiative transport model - can
835 exactly reproduce the analyzed Ly- α peak intensities and altitudes measured by the IUVS
836 instrument during MAVEN orbit 4235. This may indicate that the input parameters may not
837 accurately represent the situation in the presented case, that the cross sections used may contain
838 noticeable inaccuracies, and/or that some physical processes which are not included into the
839 models play an important role in proton aurora formation.

840 6. Conclusions and Future Work

841 The results of this modeling campaign provide a new understanding of the primary
842 factors influencing variability in Martian proton aurora. We identify the relative importance of

843 different input parameters on the proton aurora profile, finding the solar wind particle flux and
844 velocity to be the most influential parameters affecting the profile shape, brightness, and peak
845 altitude. Through undertaking this comparative study, we better constrain the driving processes
846 of proton aurora as characterized by each contributing model; additionally, we determine the
847 influence of model capabilities, solving techniques, and input assumptions on effectively
848 reproducing proton aurora observations, and the dominant physics that needs to be incorporated
849 in future modeling studies in order to accurately represent these events. Moreover, the results of
850 this study are applicable more broadly than proton aurora at Mars, as similar auroral processes
851 could occur on any planetary body that exhibits an extensive neutral H corona. Modeling studies
852 such as this one are particularly important in efforts to study planetary bodies with minimal
853 observations or where data are not available, both within our solar system and beyond (*e.g.*,
854 Venus, comets, and exoplanets).

855 In a future study, we aim to address the effects of magnetic and electric fields on proton
856 aurora. It will also be important to quantify the effect of the backscattered penetrating particle
857 population on the proton aurora profile; since the models in this study can readily take into
858 account collisional angular redistributions, incorporating these effects into the models would be
859 feasible and relevant. Evaluating the effects of the monodirectional particle movement
860 assumption (*e.g.*, by varying the incident particle bulk velocity/temperature) should also be
861 considered in a future study. We note that this study depends strongly on consideration of the
862 efficiency of charge exchange between protons in the undisturbed solar wind and H in the
863 extended corona (as this is an upper boundary for calculations due to the precipitation of H-
864 ENAs). Therefore, another possible next step for this campaign could be to consider the
865 variations present in an energy spectrum of incident H atoms and protons (*i.e.*, an energy
866 spectrum that is not monoenergetic). Additionally, major changes in the neutral atmospheric
867 scale height (*e.g.*, local or global dust storms) can affect absorption by CO₂ on the bottom side of
868 the proton aurora profile. Because absorption of Ly- α by CO₂ becomes significant below the
869 peak of the proton aurora Ly- α emitting layer, it can have a non-trivial effect on proton aurora
870 modeling efforts, potentially causing apparently lower peak intensities and higher peak altitudes
871 in proton aurora profiles. We plan to address these effects of CO₂ absorption on the proton
872 aurora profile in more detail. A future study could also potentially include creating a more
873 detailed neutral model atmosphere to use in the models (*e.g.*, including SZA variability), or
874 perhaps looking at nadir observations of proton aurora, which may help to bridge the gap
875 between *in-situ* and remote sensing observations. Finally, it would be interesting to expand our
876 analysis to include an “atypical” example of a proton aurora event in the data-modeling portion
877 of the campaign (*e.g.*, spatially and/or temporally varying, nightside detections, etc.).

878 The MAVEN mission continues to make new and exciting observations of Martian
879 proton aurora, and new Mars missions with UV instrument capabilities are also beginning to
880 make contemporaneous observations of these events. As the current solar cycle increases toward
881 solar maximum (a period corresponding with larger and more frequent solar activity), we
882 anticipate that the intensity and frequency of proton aurora events at Mars will also increase
883 correspondingly (*e.g.*, Hughes *et al.*, 2019). Thus, it is imperative in our efforts to study proton
884 aurora that we first develop a firm knowledge of the physics and driving processes through
885 modeling these events; this understanding will provide important context for future efforts to
886 effectively model new and unique auroral observations at Mars.

887

888 **Acknowledgments and Data Availability**

889 The MAVEN mission is supported by NASA through the Mars Exploration Program in
 890 association with the University of Colorado and NASA's Goddard Space Flight Center. The
 891 work of GG and BH was supported by the NASA grant 80NSSC20K1348. CSW is funded by
 892 Austrian Science Fund (FWF) project P35954-N. EK acknowledges support from the Academy
 893 of Finland (Decisions No. 348784 and No. 310444). VS and DB acknowledge the financial
 894 support of the Russian Science Foundation, grant # 22-12-00364. JCG acknowledges support
 895 from the PRODEX program of ESA managed with the help of the Belgian Federal Scientific
 896 Policy Office (BELSPO).

897 In this study we use MAVEN/IUVS Level 1C version 13 altitude-binned periapsis data.
 898 This work utilized the RMACC Summit supercomputer, which is supported by the National
 899 Science Foundation (awards ACI-1532235 and ACI-1532236), the University of Colorado
 900 Boulder, and Colorado State University. The Summit supercomputer is a joint effort of the
 901 University of Colorado Boulder and Colorado State University.

902 All daytime Level 1C IUVS data products are publicly available from the Planetary
 903 Atmospheres node of the Planetary Data System (PDS) ([https://pds-
 904 atmospheres.nmsu.edu/data_and_services/atmospheres_data/MAVEN/maven_iuvs.html](https://pds-atmospheres.nmsu.edu/data_and_services/atmospheres_data/MAVEN/maven_iuvs.html)).
 905 Similarly, MAVEN/SWIA ([https://pds-
 906 atmospheres.nmsu.edu/data_and_services/atmospheres_data/MAVEN/swia.html](https://pds-atmospheres.nmsu.edu/data_and_services/atmospheres_data/MAVEN/swia.html)) and
 907 MAVEN/NGIMS ([https://pds-
 908 atmospheres.nmsu.edu/data_and_services/atmospheres_data/MAVEN/ngims.html](https://pds-atmospheres.nmsu.edu/data_and_services/atmospheres_data/MAVEN/ngims.html)) data are also
 909 available from the PDS. All MAVEN instrument Software Interface Specification (SIS)
 910 documents can be found on the before-mentioned PDS websites. The ATMOCIAAD (Atomic and
 911 Molecular Cross section for Ionization and Aurora Database) database used in the Aeroplanets
 912 model (Gronoff *et al.*, 2021) is available at <https://doi.org/10.5281/zenodo.4632426>.

913 We would like to thank our collaborators on the MAVEN and IUVS Teams, especially
 914 Meredith Elrod and Robin Ramstad, for their contributions in understanding the local Mars
 915 environment during the time period of interest.

916

917 **References**

- 918 Anderson, D. E., and Hord, C. W. (1971). Mariner 6 and 7 Ultraviolet Spectrometer Experiment:
 919 Analysis of hydrogen Lyman-alpha data, *J. Geophys. Res.*, 76 (28), 6666– 6673,
 920 doi:10.1029/JA076i028p06666.
- 921 Bertaux, J.-L., Leblanc, F., Witasse, O., Quemerais, E., Lilensten, J., Stern, S. A., ... Korablev,
 922 O. (2005), Discovery of an aurora on Mar, *Nature*, 435(7043), 790–794, doi:
 923 10.1038/nature03603.
- 924 Bisikalo D.V., Shematovich V.I., Gérard J.-C., Hubert B. (2018), Monte Carlo simulations of the
 925 interaction of fast proton and hydrogen atoms with the Martian atmosphere and
 926 comparison with in situ measurements, *Journal of Geophysical Research: Space Physics*,
 927 V. 123, Issue 7, pp. 5850-5861.

- 928 Chaffin, M. S., J.-Y. Chaufray, I. Stewart, F. Montmessin, N. M. Schneider, and J.-L. Bertaux
929 (2014), Unexpected variability of Martian hydrogen escape, *Geophysical Research*
930 *Letters*, 41(2), 314-320, doi:10.1002/2013gl058578.
- 931 Chaffin, M.S., Kass, D.M., Aoki, S. et al. Martian water loss to space enhanced by regional dust
932 storms. *Nat Astron* 5, 1036–1042 (2021). <https://doi.org/10.1038/s41550-021-01425-w>
- 933 Clarke, J. T., J. L. Bertaux, J. Y. Chaufray, G. R. Gladstone, E. Quémerais, J. Wilson, and D.
934 Bhattacharyya (2014), A rapid decrease of the hydrogen corona of Mars, *Geophysical*
935 *Research Letters*, 41(22), 8013-8020.
- 936 Deighan, J, S. K. Jain, M. S. Chaffin, X. Fang, J. S. Halekas, J. T. Clarke, N. M. Schneider, A. I.
937 F. Stewart, J.-Y. Chaufray, J. S. Evans, M. H. Stevens, M. Mayyasi, A. Stiepen, M.
938 Crismani, W. E. McClintock, G. M. Holsclaw, D. Y. Lo, F. Montmessin, F. Lefevre, B.
939 M. Jakosky (2018), Discovery of Proton Aurora at Mars, *Nature Astronomy*, 2(10), 802.
- 940 England, S. L., Liu, G., Withers, P., Yiğit, E., Lo, D., Jain, S., ... and Elrod, M., (2016),
941 Simultaneous observations of atmospheric tides from combined in situ and remote
942 observations at Mars from the MAVEN spacecraft, *J. Geophys. Res.: Planets*, Volume
943 121, Issue 4, pp. 594-607.
- 944 Galand, M., J. Lilensten, W. Kofman, and R. B. Sidje (1997), Proton transport model in the
945 ionosphere 1. Multistream approach of the transport equations, *Journal of Geophysical*
946 *Research*, 102, 22261–72, <https://doi.org/10.1029/97JA01903>.
- 947 Galand, M., J. Lilensten, W. Kofman, and D. Lummerzheim (1998), Proton transport model in
948 the ionosphere. 2. Influence of magnetic mirroring and collisions on the angular
949 redistribution in a proton beam, *Annales Geophysicae*, 16, 1308–21,
950 <https://doi.org/10.1007/s00585-998-1308-y>.
- 951 Gérard J.-C., Hubert B., Bisikalo D.V., and Shematovich V.I. (2000), Lyman-alpha emission in
952 the proton aurora. *J. Geophys. Res.*, V. 105, No. A7, 15795.
- 953 Gérard, J. C., B. Hubert, B. Ritter, V. I. Shematovich, D. V. Bisikalo (2019), Lyman- α emission
954 in the Martian proton aurora: Line profile and role of horizontal induced magnetic field,
955 *Icarus*, 321, 266-271.
- 956 Girazian and Halekas (2021), Precipitating Solar Wind Hydrogen at Mars: Improved
957 Calculations of the Backscatter and Albedo with MAVEN Observations, *J. Geophys.*
958 *Res.: Planets*, Volume 126, Issue 2, doi: 10.1029/2020JE006666.
- 959 Gronoff, G., C. Simon Wedlund, C. J. Mertens, and R. J. Lillis (2012a), “Computing
960 uncertainties in ionosphere-airglow models: I. Electron flux and species production
961 uncertainties for Mars”, *Journal of Geophysical Research: Space Physics*, 117 (April):
962 4306, 18 PP., <https://doi.org/10.1029/2011JA016930>.
- 963 Gronoff, G., C. Simon Wedlund, C. J. Mertens, M. Barthélemy, R. J. Lillis, and O. Witasse
964 (2012b), “Computing Uncertainties in Ionosphere-Airglow Models: II. The Martian
965 Airglow”, *J. Geophys. Res.* 117 (May): 17 PP.
966 <https://doi.org/10.1029/2011JA017308>.
- 967 Gronoff, G., B. Hegyi, C. Simon Wedlund, & J. Lilensten. (2021), “The ATMOCIAAD database”,
968 *Zenodo*. <https://doi.org/10.5281/zenodo.4632426>

- 969 Halekas, J. S., E. R. Taylor, G. Dalton, G. Johnson, D. W. Curtis, J. P. McFadden, D. L.
 970 Mitchell, R. P. Lin, B. M. Jakosky (2013), The Solar Wind Ion Analyzer for MAVEN,
 971 *Space Science Rev.*, 195(1-4), 125-151.
- 972 Halekas, J. S., Lillis, R. J., Mitchell, D. L., Cravens, T. E., Mazelle, C., Connerney, J. E. P., ... &
 973 Luhmann, J. G. (2015), MAVEN observations of solar wind hydrogen deposition in the
 974 atmosphere of Mars, *Geophys. Res. Lett.*, 42, 8901–8909, doi: 10.1002/2015GL064693.
- 975 Halekas, J. S. (2017), Seasonal variability of the hydrogen exosphere of Mars, *J. Geophys. Res.:*
 976 *Planets*, 122, 901–911, doi: 10.1002/2017JE005306.
- 977 Henderson, S., Halekas, J., Girazian, Z., Espley, J., & Elrod, M. (2022), Influence of magnetic
 978 fields on precipitating solar wind hydrogen at Mars, *Geophysical Research Letters*, 49,
 979 e2022GL099114. <https://doi.org/10.1029/2022GL099114>.
- 980 Huestis, D.L., and J. Berkowitz, (2010). Critical evaluation of the photoabsorption cross section
 981 of CO₂ from 0.125 to 201.6 nm at room temperature, *Advances in Geosciences Vol. 25:*
 982 *Planetary Science* 229-242
- 983 Hughes, A., Chaffin, M., Mierkiewicz, E., Deighan, J., Jain, S., Schneider, N., (2019), Proton
 984 aurora on Mars: A dayside phenomenon pervasive in southern summer, *J. Geophys. Res.:*
 985 *Space Physics*, 124, 10,533–10,548, doi: 10.1029/2019JA027140.
- 986 Hunten, D.M., F.E. Roach, and J.W. Chamberlain, (1956). A photometric unit for the airglow
 987 and aurora, *Journal of Atmospheric and Terrestrial Physics*, Volume 8, Issue 6, Pages
 988 345-346, [https://doi.org/10.1016/0021-9169\(56\)90111-8](https://doi.org/10.1016/0021-9169(56)90111-8).
- 989 Jakosky, B. M., Lin, R. P., Grebowsky, J. M., Luhmann, J. G., Mitchell, D. F., Beutelschies, G.,
 990 ... & Baker, D. (2015), The Mars atmosphere and volatile evolution (MAVEN) mission,
 991 *Space Sci. Rev.*, 195(1-4), 3-48.
- 992 Jolitz, R. D., C. F. Dong, C. O. Lee, R. J. Lillis, D. A. Brain, S. M. Curry, S. Bougher, C. D.
 993 Parkinson, and B. M. Jakosky (2017), A Monte Carlo model of crustal field influences on
 994 solar energetic particle precipitation into the Martian atmosphere, *J. Geophys. Res. Space*
 995 *Physics*, 122, 5653–5669, doi:10.1002/2016JA023781.
- 996 Jolitz, R. D., Dong, C. F., Rahmati, A., Brain, D. A., Lee, C. O., Lillis, R. J., Curry, and B. M.
 997 Jakosky (2021), Test particle model predictions of SEP electron transport and
 998 precipitation at Mars, *Journal of Geophysical Research: Space Physics*, 126,
 999 e2021JA029132, <https://doi.org/10.1029/2021JA029132>
- 1000 Kallio, E., and S. Barabash (2000), On the elastic and inelastic collisions between precipitating
 1001 energetic hydrogen atoms and Martian atmospheric neutrals [J. Geophys. Res., 105,](https://doi.org/10.1029/2000JA002003)
 1002 [24,973-24,996.](https://doi.org/10.1029/2000JA002003)
- 1003 Kallio, E., & Barabash, S. (2001), Atmospheric effects of precipitating energetic hydrogen atoms
 1004 on the Martian atmosphere, *J. Geophys. Res.:* *Space Physics*, 106(A1), 165-177, doi:
 1005 10.1029/2000JA002003.
- 1006 Lo, D. Y., Yelle, R. V., Schneider, N. M., Jain, S. K., Stewart, A. I. F., England, S. L., ... &
 1007 Chaffin, M. S. (2015), Nonmigrating tides in the Martian atmosphere as observed by
 1008 MAVEN IUVS, *Geophys. Res. Lett.*, 42(21), 9057-9063.

- 1009 Mahaffy, P.R., Benna, M., King, T. *et al.* The Neutral Gas and Ion Mass Spectrometer on the
1010 Mars Atmosphere and Volatile Evolution Mission. *Space Sci Rev* **195**, 49–73 (2015).
1011 <https://doi.org/10.1007/s11214-014-0091-1>
- 1012 McClintock, W. E., N. M. Schneider, G. M. Holsclaw, J. T. Clarke, A. C. Hoskins, I. Stewart, F.
1013 Montmessin, R. V. Yelle (2015), The Imaging Ultraviolet Spectrograph (IUVS) for the
1014 MAVEN Mission, *Space Sci. Rev.*, doi: 10.1007/s11214-014-0098-7.
- 1015 Ritter, B., J.-C. Gérard, B. Hubert, L. Rodriguez, and F. Montmessin (2018), Observations of the
1016 proton aurora on Mars with SPICAM on board Mars Express, *Geophys. Res. Lett.*, 45.
1017 doi: 10.1002/2017GL076235.
- 1018 Schneider, N. M., J. I. Deighan, S. K. Jain, A. Stiepen, A. I. F. Stewart, D. Larson, D. L.
1019 Mitchell, C. Mazelle, C. O. Lee, and R. J. Lillis (2015), Discovery of diffuse aurora on
1020 Mars, *Science*, 350(6261), aad0313.
- 1021 Shematovich V. I., D. V. Bisikalo, C. Diéval, S. Barabash, G. Stenberg, H. Nilsson, Y. Futaana,
1022 M. Holmstrom, and J.-C. Gérard. (2011), Proton and hydrogen atom transport in the
1023 Martian upper atmosphere with an induced magnetic field, *J. Geophys. Res.*, V. 116,
1024 Issue A11, CiteID A11320.
- 1025 Shematovich V.I., Bisikalo D.V., Gérard J.-C., Hubert B. (2019), Kinetic Monte Carlo model of
1026 the precipitation of high-energy proton and hydrogen atoms into the Martian atmosphere
1027 with taking into account the measured magnetic field, *Astronomy Reports*, Vol. 63, No.
1028 10, pp. 835–845.
- 1029 Simon, Cyril. (2006), “Contribution à L’étude Des Entrées d’énergie Solaire Dans L’ionosphère:
1030 Ions Doublement Chargés et Transport Cinétique Des Protons - Application à La Terre et
1031 à Titan.” PhD thesis, Université Joseph-Fourier - Grenoble I. [http://tel.archives-](http://tel.archives-ouvertes.fr/tel-00109802)
1032 [ouvertes.fr/tel-00109802](http://tel.archives-ouvertes.fr/tel-00109802).
- 1033 Simon, C., J. Lilensten, J. Moen, J. M. Holmes, Y. Ogawa, K. Oksavik, and W. F. Denig (2007),
1034 “TRANS4: a new coupled electron/proton transport code - comparison to observations
1035 above Svalbard using ESR, DMSP and optical measurements.” *Annales Geophysicae* 25
1036 (March): 661–73. <https://doi.org/10.5194/angeo-25-661-2007>.
- 1037 Simon Wedlund, C., G. Gronoff, J. Lilensten, H. Ménager, and M. Barthélemy (2011),
1038 “Comprehensive calculation of the energy per ion pair or W values for five major
1039 planetary upper atmospheres.” *Annales Geophysicae* 29 (January): 187–95.
1040 <https://doi.org/10.5194/angeo-29-187-2011>.
- 1041 Stone, S. W., Yelle, R. V., Benna, M., Elrod, M. K., & Mahaffy, P. R. (2018), Thermal structure
1042 of the Martian upper atmosphere from MAVEN NGIMS. *Journal of Geophysical Research: Planets*, 123,
1043 2842–2867. <https://doi.org/10.1029/2018JE005559>.